Laser & Photonics Reviews

LASER & PHOTONICS REVIEWS

www.lpr-journal.org

RESEARCH ARTICLE

Ultra-Narrow and Stable Blue Perovskite LEDs Enabled by Synergistic Interfacial Modulation With Multifunctional Molecular Bridges

Longqi Lin[1] | Jihong Wu[2] | Zhibin Wang[1] | Song Zheng[1] | Zhehong Zhou[1] | Xin Zhou[1] | Mingwei An[2] | Yang Wang[2] | Lingwei Zeng[3] | Ruidan Zhang[1] | Daqin Chen[1,4]

[1]College of Physics and Energy, Fujian Normal University, Fuzhou, Fujian, People's Republic of China | [2]Strait Laboratory of Flexible Electronics (SLoFE), Fujian Key Laboratory of Flexible Electronics, Strait Institute of Flexible Electronics (SIFE, Future Technologies), Fujian Normal University, Fuzhou, Fujian, People's Republic of China | [3]School of Chemistry and Chemical Engineering, Hunan University of Science and Technology, Xiangtan, Hunan, People's Republic of China | [4]Fujian Provincial Engineering Technology Research Center of Solar Energy Conversion and Energy Storage, Fujian Normal University, Fuzhou, Fujian, People's Republic of China

Correspondence: Zhibin Wang (zhibinwang@fjnu.edu.cn) | Yang Wang (ifewangy@fjnu.edu.cn) | Daqin Chen (dqchen@fjnu.edu.cn)

Received: 1 June 2026 | **Revised:** 15 August 2026 | **Accepted:** 21 August 2026

Keywords: buried interface | donor–acceptor molecules | energetic disorder | molecular bridge | perovskite light-emitting diodes

ABSTRACT

High-color-purity blue perovskite light-emitting diodes (PeLEDs) using wide bandgap quasi-two-dimensional (quasi-2D) perovskites are limited by buried interface disorder, poor hole injection, broad phase distribution, and nonradiative losses. Here, terminal benzoic-acid-functionalized donor–acceptor (D–A) molecules, MPA-BT-BA (0F) and fluorinated MPA2FPh-BT-BA (2F), are introduced into the hole transport layer as molecular bridges. They reduce energetic disorder in poly(9-vinylcarbazole) (PVK), facilitate hole transport, coordinate Pb^{2+} precursor species, promote interfacial nucleation, and passivate Pb defects. Fluorinated 2F further strengthens hydrogen bonding with organic spacer cations, suppressing low-n phases, narrowing phase distribution, and directing energy transfer to the dominant emissive phase. Devices achieve 9.3% external quantum efficiency at 478 nm, an 80 meV (14.73 nm) ultranarrow electroluminescence linewidth, 2.0 V turn-on voltage, and 41.9 min T_{50} lifetime at 100 cd m^{-2}, highlighting molecular bridge interface engineering for low-voltage, color-pure, and operationally stable blue PeLEDs.

1 | Introduction

Metal halide perovskites are promising semiconductors for next-generation light-emitting diodes because of their tunable bandgaps, narrow-band emission, high color purity, and low-cost solution processability. Green and red perovskite light-emitting diodes (PeLEDs) have already achieved external quantum efficiencies (EQEs) above 30% [1–5]. In contrast, blue PeLEDs, especially those with emission below 480 nm, still lag far behind in efficiency and spectral purity. This spectral region is critical for full-color displays, governing color gamut, color purity, and stability in next-generation high-resolution technologies [6–9].

Among the available strategies, quasi-two-dimensional (quasi-2D) perovskites are attractive for blue emission because their quantum and dielectric confinement can enhance exciton binding and radiative recombination through energy funneling [10]. However, the performance of blue quasi-2D PeLEDs is highly sensitive not only to phase distribution in the emissive layer, but also to the buried interface [11, 12]. The deeper valence band of

Longqi Lin and Jihong Wu contributed equally to this work.

blue perovskites often causes hole injection barriers, while the mixed-halide composition and quasi-2D phase distribution make precursor coordination, nucleation, and phase evolution highly interface-dependent [13, 14]. As a result, poor interfacial wetting and pronounced energetic disorder at the interface can induce enrichment of low-*n* phases, trap formation, spectral broadening, and device instability [15]. Therefore, an integrated interfacial strategy is needed to simultaneously regulate charge injection, crystallization, phase distribution, and defect evolution in blue quasi-2D PeLEDs.

To address these challenges, substantial progress has been made through interfacial molecular design and crystallization kinetics control. For example, Chu and co-workers used the multifunctional p-type molecule (2-(3,6-dibromo-9H-carbazol-9-yl)ethyl)phosphonic acid (Br-2PACz) to induce spontaneous vertical phase separation, forming a deep-HOMO transport layer at the perovskite/transport-layer interface that reduces the hole injection barrier and improves charge balance in blue PeLEDs [16]. Zhou et al. introduced Cl-rich benzene phosphorus oxydichloride (BPOD) for in situ hydrolysis, generating passivating species that coordinate undercoordinated Pb^{2+}, repair halide-vacancy defects, and suppress ion migration [17]. Qi et al. combined formamidinium tetrafluorosuccinate (FATFSA) with a 2-methacryloyloxyethyl phosphorylcholine (MPC) interfacial layer to suppress unfavorable low-dimensional phases, homogenize the energy landscape, and promote energy transfer [18]. Despite their effectiveness, these strategies mainly focus on perovskite-side or interfacial regulation, while the intrinsic properties of the underlying hole transport layer (HTL) have received comparatively less attention. Poly(9-vinylcarbazole) (PVK) is widely used as a hole transport material in blue PeLEDs because of its good film-forming ability and deep-lying energy levels [19]. Nevertheless, its intrinsic energetic disorder and poor contact with the overlying perovskite can still cause injection barriers and nonuniform crystallization at the buried interface [20]. Therefore, a single-molecule bridging strategy that simultaneously reduces PVK energetic disorder, regulates precursor coordination, guides perovskite crystallization, suppresses low-n phase formation, and passivates interfacial defects at the PVK/quasi-2D perovskite buried interface is highly desirable.

In this work, we design two donor–acceptor (D–A) molecules with terminal benzoic-acid anchoring moieties, MPA-BT-BA (0F) and its fluorinated analogue MPA2FPh-BT-BA (2F), and incorporate them into the PVK HTL through solution blending. At the PVK/perovskite buried interface, these D–A molecules function as molecular bridges, where π–π interactions with PVK reduce energetic disorder and trap-related states in the HTL, thereby mitigating hole-injection energy losses, while carboxylate–Pb^{2+} coordination regulates precursor coordination, crystallization, and phase distribution in the overlying perovskite. In 2F, fluorination further strengthens hydrogen-bonding interactions with organic spacer cations, thereby regulating organic-cation assembly and suppressing low-*n* phase formation. Devices based on the D–A molecular-bridge architecture show a low turn-on voltage (V_T) of 2.0 V (≈77% of the 2.6 V bandgap voltage), an ultranarrow electroluminescence (EL) linewidth of 80 meV (14.73 nm), and a T_{50} operational lifetime of 41.9 min at 100 cd m^{-2}. These results position D–A molecular bridge design as a valuable principle for multifunctional buried-interface regulation in blue PeLEDs.

2 | Results and Discussion

D–A molecules bearing anchoring end groups can simultaneously tune the organic HTL and inorganic perovskite interface [21, 22]. Accordingly, we designed two anchoring-group-functionalized D–A molecules, 0F and fluorinated 2F, both comprising donor, acceptor, and terminal benzoic-acid anchoring units but differing in substitution pattern (Figure 1a) [23]. Both molecules contain three key components: a donor unit, an acceptor unit, and a terminal benzoic-acid anchoring group. The dimethoxy-substituted aryl group promotes intermolecular interactions with PVK chains, the benzothiadiazole acceptor adjusts intramolecular charge distribution and interfacial polarity, and the carboxylate group of the terminal benzoic-acid moiety provides a coordination site for undercoordinated Pb^{2+}.

Compared with 0F, fluorinated 2F redistributes the electrostatic potential (ESP) and generates defined electronegative regions. The calculated dipole moment decreases from 7.41 D for 0F to 6.35 D for 2F (Figure S1), indicating that fluorination mainly reshapes the local ESP distribution rather than increasing the overall molecular polarity. Consistently, low-dipole fluorinated regulators have been shown to modulate quasi-2D phase distribution through local interactions with spacer cations [24]. Frontier-orbital analysis shows that fluorination downshifts the HOMO/LUMO levels from −5.05/−2.74 eV for 0F to −5.21/−2.89 eV for 2F (Figure S2), suggesting tuned electrostatic and electronic structures that support stronger interfacial regulation [25]. Nuclear magnetic resonance (NMR) spectroscopy further confirms both structures (Figure S3).

As illustrated in Figure 1b, 0F and 2F were uniformly blended with PVK in N,N-dimethylformamide (DMF), yielding smooth PVK:0F and PVK:2F composite films on ITO/poly[bis(4-phenyl)(2,4,6-trimethylphenyl)amine] (PTAA) substrates. The perovskite emissive layer (EML) was subsequently deposited from a precursor solution using dimethyl sulfoxide (DMSO) as the solvent. Owing to their high DMSO solubility, 0F and 2F remain well dispersed during perovskite deposition, facilitating uniform interfacial modification.

To verify the interfacial interactions suggested above, we carried out X-ray photoelectron spectroscopy (XPS) on perovskite films deposited on different HTLs. Modification with 0F or 2F shifts the Pb 4*f* core-level peaks to lower binding energies (Figure 1c). The Pb $4f_{5/2}$ peak moves from 142.1 eV in the PVK-based film to 142.0 eV for PVK:0F and 141.7 eV for PVK:2F, accompanied by a Pb $4f_{7/2}$ shift from 137.14 to 137.02 eV and 136.82 eV, respectively. These shifts indicate increased electron density at Pb^{2+} sites, supporting carboxylate–Pb^{2+} coordination and the passivation of Pb-related interfacial defects [26].

Fourier transform infrared (FTIR) spectroscopy provides further evidence of interactions between the D–A molecules and the precursor species. 0F and 2F display characteristic ν(C═O) bands at 1678 and 1689 cm^{-1}, respectively, without a clear $\nu(COO^-)$ signal. After mixing with $PbBr_2$, the ν(C═O) band of 0F shifts to 1682 cm^{-1} and a new $\nu(COO^-)$ band appears at 1371 cm^{-1}. For 2F, the ν(C═O) band shifts to 1686 cm^{-1}, accompanied by

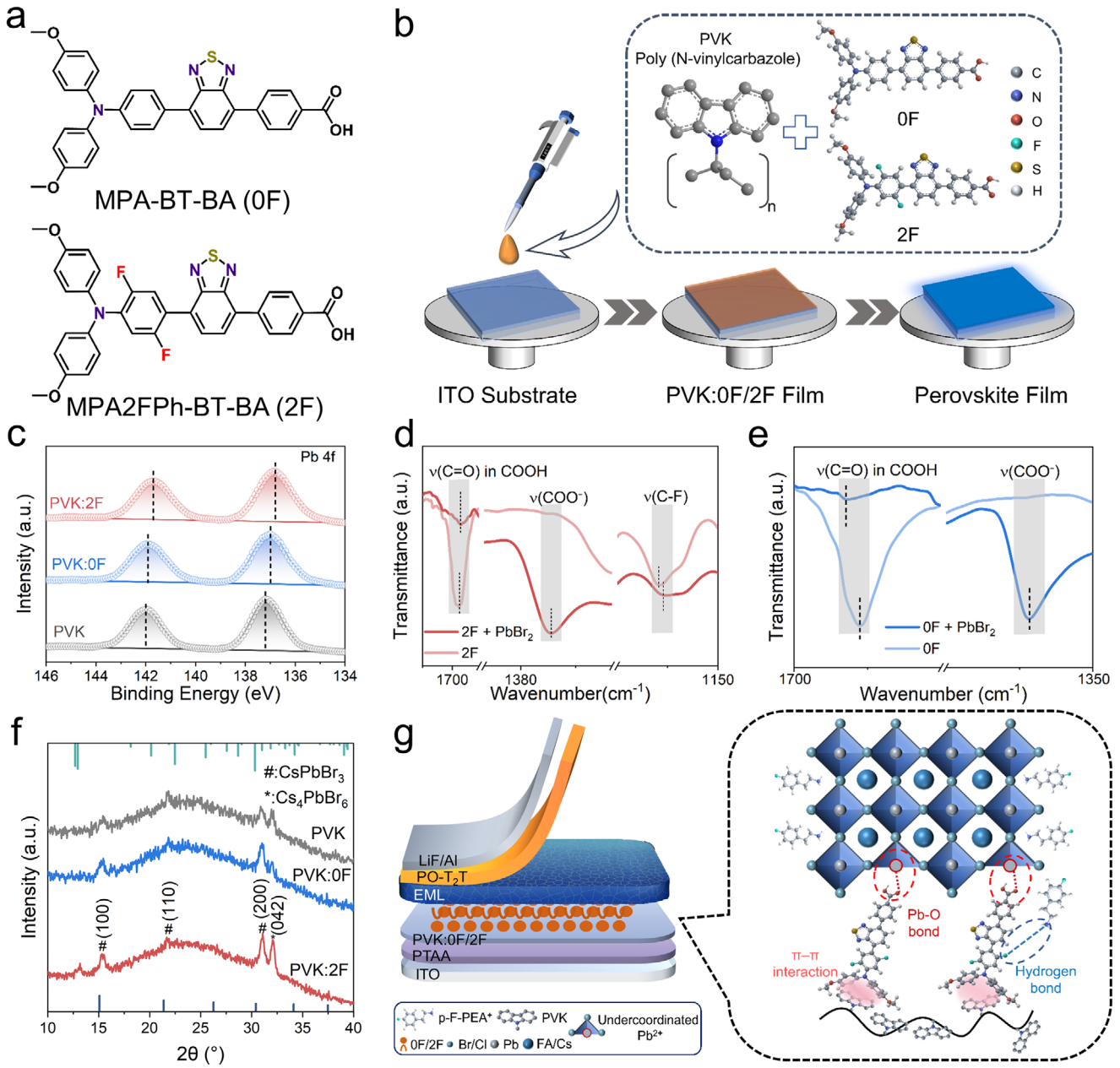

FIGURE 1 | Molecular design and buried interface mechanism of 0F/2F. (a) Chemical structures of MPA-BT-BA (0F) and MPA2FPh-BT-BA (2F). (b) Fabrication of the 0F/2F-modified buried interface. (c) Pb 4*f* XPS spectra of PVK, PVK:0F, and PVK:2F. (d,e) Fourier transform infrared (FTIR) spectra of 0F/2F with and without $PbBr_2$. (f) XRD patterns of perovskite films on PVK, PVK:0F, and PVK:2F substrates. (g) Device architecture and proposed D–A molecular bridge mechanism.

the emergence of a $\nu(COO^-)$ band at 1370 cm^{-1} (Figure 1d,e). These changes confirm coordination between both molecules and undercoordinated Pb^{2+} sites through their carboxylate groups [27].

Notably, the ν(C–F) shift of 2F from 1180 to 1177 cm^{-1} after $PbBr_2$ addition suggests that Pb–carboxylate coordination perturbs the fluorinated backbone, helping regulate interfacial precursor coordination [28]. Additional FTIR data show stronger coupling between 2F and phenethylammonium cations (PEA^+), as evidenced by a 38 cm^{-1} redshift of ν(N–H) and a concurrent ν(C–F) shift (Figure S4), indicating hydrogen-bonding interactions between the fluorine atoms in 2F and the N–H groups of PEA^+. These results suggest that 2F combines carboxylate binding to Pb^{2+} sites with spacer-cation hydrogen bonding to improve crystallization control [29].

X-ray diffraction (XRD) patterns were then collected to examine how these D–A molecules affect film crystallization (Figure 1f). All samples retain the characteristic diffraction peaks of the $CsPbBr_3$ phase, indicating that introducing 0F or 2F does not disrupt the perovskite framework or lead to lattice incorporation. The diffraction peaks also shift slightly to higher angles, consistent with lattice contraction caused by Cl incorporation. Compared with the control film, the 0F-treated film shows stronger diffraction peaks, while the 2F-treated film exhibits the

most pronounced enhancement and clearer reflections from the crystal planes, indicating improved crystallinity and structural order. A weak peak at 12.6° is assigned to the FABr-induced $Cs_4PbCl_6Br_{6-x}$ phase, consistent with previous reports [30]. These results indicate that 0F and 2F mainly optimize precursor coordination and nucleation behavior at the buried interface.

Thus, 0F and 2F act as molecular bridges between PVK and perovskite at the buried interface, with π–π stacking interactions reducing energetic disorder in PVK and terminal carboxylate coordination with undercoordinated Pb^{2+} regulating precursor coordination and promoting uniform nucleation (Figure 1g). In 2F, hydrogen bonding between fluorinated sites and the N–H groups of PEA^+ further stabilizes spacer-cation assembly and directs quasi-2D phase distribution, enabling simultaneous regulation of inorganic coordination and organic assembly, more uniform crystallization and reduced interfacial energetic disorder.

To clarify how the D–A molecular bridges regulate the buried interface during the early stages of film formation, we used scanning electron microscopy (SEM) to examine their effects on perovskite growth. Before perovskite deposition, atomic force microscopy (AFM) measurements showed that the RMS roughness decreased from 2.41 nm for PVK to 1.69 nm and 1.52 nm for PVK:0F and PVK:2F, respectively (Figure S5), indicating smoother HTL surfaces after molecular incorporation. The control film deposited on PVK exhibits clear pinholes and discontinuous regions, indicating poor precursor spreading and nonuniform nucleation on this surface (Figure 2a–c). Introducing 0F yields a more uniform film morphology, while 2F further improves film formation, producing the most compact and continuous film. Consistently, the DMSO contact angle decreases from 40.5° on PVK to 30.7° on PVK:0F and 28.5° on PVK:2F (Figure S6), indicating improved precursor wettability, stronger interfacial affinity, and more effective precursor spreading on the 2F-modified surface.

The buried interface is particularly important in blue PeLEDs because it governs initial precursor coverage and defect formation [31]. Buried interface SEM images show voids and discontinuities in the PVK control, indicating insufficient precursor coverage and defect-prone initial crystallization (Figure 2d–f). These morphological defects are reduced after 0F modification, while 2F yields a smooth, continuous buried interface with almost no large voids. These observations indicate that 2F improves HTL/precursor compatibility and promotes uniform interfacial nucleation, thereby suppressing defect formation during early film growth.

Beyond the morphological changes, Kelvin probe force microscopy (KPFM) was used to map the spatial distribution of surface potential across the films. Pronounced surface-potential fluctuations are observed for the PVK film, whereas incorporating 0F or 2F yields a more uniform potential landscape; the corresponding statistical distributions of the contact potential difference (CPD) are shown in the insets (Figure 2g–i). Gaussian fitting shows that the full width at half maximum (FWHM) of the CPD distribution decreases from 35.1 mV for PVK to 27.1 mV for PVK:0F and further to 25.6 mV for PVK:2F. This CPD narrowing indicates that D–A molecular bridges reduce surface-potential variations and smooth the interfacial energy landscape, supporting more uniform hole injection [32, 33].

To validate this interpretation, hole-only devices with the structure ITO/PTAA/X/EML/MoO_3/Ag (X = PVK, PVK:0F or PVK:2F) were analyzed by space-charge-limited current (SCLC) measurements (Figure S7). The trap-filled limit voltages (V_{TFL}) decrease from 0.84 V for PVK to 0.68 V for PVK:0F and 0.64 V for PVK:2F, corresponding to trap-state densities (N_t) of 1.45×10^{18}, $1.18 \times 10^{18,}$ and 1.11×10^{18} cm^{-3}, respectively. Meanwhile, PVK:2F shows the highest hole mobility (μ_h) of 6.2×10^{-6} $cm^2 V^{-1} s^{-1}$, exceeding those of PVK:0F and PVK by 1.2 and 5.2 times, respectively [34]. These results indicate that D–A molecular bridges reduce the trap-state density near the buried interface and improve hole transport.

To probe the influence of D–A molecules on phase distribution and excited-state dynamics, femtosecond transient absorption (fs-**TA**) measurements were performed on perovskite films deposited on different HTLs. All films show bleaching signals across 400–500 nm, but the PVK film exhibits broad, overlapping features from multiple n phases. These features become more concentrated with 0F and are centered near the 475 nm emissive phase with 2F, indicating a narrowed phase distribution and a more focused excited-state relaxation pathway (Figure 3a–c).

As low-n phase distribution strongly affects quasi-2D PeLEDs performance, we next examined the phase composition of these films. The steady-state **UV**–vis spectra show distinct $n = \mathbf{2}$ and $n = \mathbf{3}$ absorption features in the perovskite film on pristine PVK (Figure S8). These low-n features are strongly suppressed by 0F and nearly eliminated by 2F. Consistently, the fs-TA spectra of the PVK-based film display three ground-state bleaching (GSB) features at 415, 445, and 475 nm, which are assigned to the $n = 2$, $n = \mathbf{3}$ and $n \geq \mathbf{4}$ phases, respectively (Figure 3d–f). The coexistence of these signals at early delay times indicates a broadly distributed initial excited-state population and energy transfer across multiple phase domains. In the PVK:0F film, the contribution from the low-n phases is reduced. By contrast, the PVK:2F film is already dominated by the $n \geq \mathbf{4}$ phase at very early delay times and remains highly consistent during subsequent evolution. The relative phase populations shown in the insets are supported by Gaussian peak deconvolution (Figure S9) [35].

Whereas the pristine PVK film retains clear multiphase coexistence at both 0.4 and 1 ps, the PVK:0F film shows a weaker low-n contribution and a gradual shift of the excited-state population toward the high-n phase. In the PVK:2F film, however, the $n \geq \mathbf{4}$ phase dominates as early as 0.4 ps and remains stable at 1 ps, indicating that 2F compresses the initial excited-state distribution and promotes rapid energy concentration into the dominant emissive phase.

To further define the energy transfer process, kinetic traces for the different GSB signals were extracted and fitted. The decay time constant (τ_1) of the $n = \mathbf{3}$ phase decreases from 0.25 ps in PVK to 0.19 ps in PVK:0F and 0.14 ps in PVK:2F, indicating progressively accelerated energy transfer from low-n to high-n phases (Figure S10 and Table S2). Consistently, the formation time constant (τ_{et}) of the $n \geq \mathbf{4}$ phase shortens from 0.50 to 0.22 ps and then to 0.16 ps. Together, these results show that both 0F and 2F

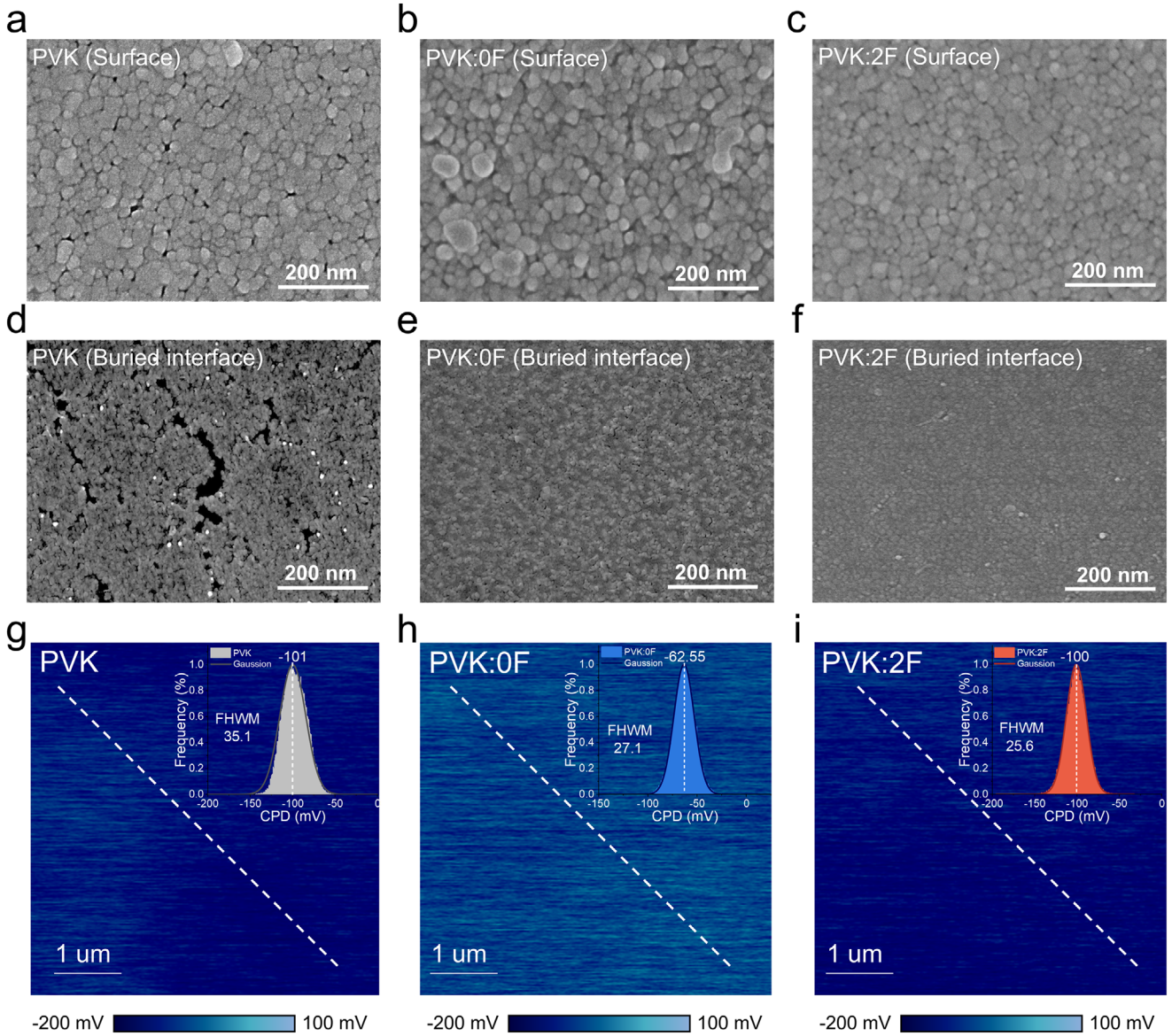

FIGURE 2 | Morphology and surface potential distribution of PVK, PVK:0F and PVK:2F films. (a–c) Top-view SEM images. (d–f) Buried-interface SEM images. (g–i) KPFM images with Gaussian-fitted contact potential difference (CPD) histograms and full width at half maximum (FWHM) values.

accelerate exciton transfer toward the high-*n* phase. This faster and more directed energy funneling is expected to favor radiative recombination in the dominant emissive phase [36].

In addition to reshaping the phase distribution of the emissive layer, the D–A molecules also regulate the electronic-state distribution of the HTL. Ultraviolet photoelectron spectroscopy (UPS) reveals that, relative to pristine PVK, the HOMO onset becomes progressively steeper after modification with 0F and 2F, accompanied by a clear reduction in tail states and a slight deepening of the HOMO level (Figure 3g–i). These changes indicate a more concentrated density of states near the HOMO edge and reduced electronic disorder [37]. To quantify this trend, the HOMO-onset width (σ_{UPS}) was extracted by Gaussian fitting after background correction and intensity normalization, as described in the Supporting Information. Consistently, σ_{UPS} decreases from 0.96 ± 0.01 eV for PVK to 0.79 ± 0.01 eV for PVK:0F and further to 0.73 ± 0.01 eV for PVK:2F, confirming that 2F most effectively suppresses tail-state broadening and reduces energetic disorder in the HTL [38]. **2**F therefore delivers complementary interfacial regulation on both sides of the device, suppressing low-*n* phases and promoting rapid energy funneling into the dominant emissive phase on the perovskite side, while reducing energetic disorder in the HTL.

Consistent with the narrower phase distribution and smoother interfacial energy landscape described above, the D–A molecules also produce a clear improvement in the photoluminescence properties of the perovskite films. Both 0F and 2F enhance the photoluminescence (PL) intensity, with the 2F-modified film showing the strongest emission. It also exhibits a narrower linewidth of 14.1 nm and a higher photoluminescence quantum yield (PLQY) of 34.97%, compared with 15.5 nm and 3.73% for the PVK film (Figure 4a,b and Figure S11). Tri-exponential fitting of the time-resolved photoluminescence (TRPL) decay curves shows a longer average PL lifetime for PVK:2F than for PVK

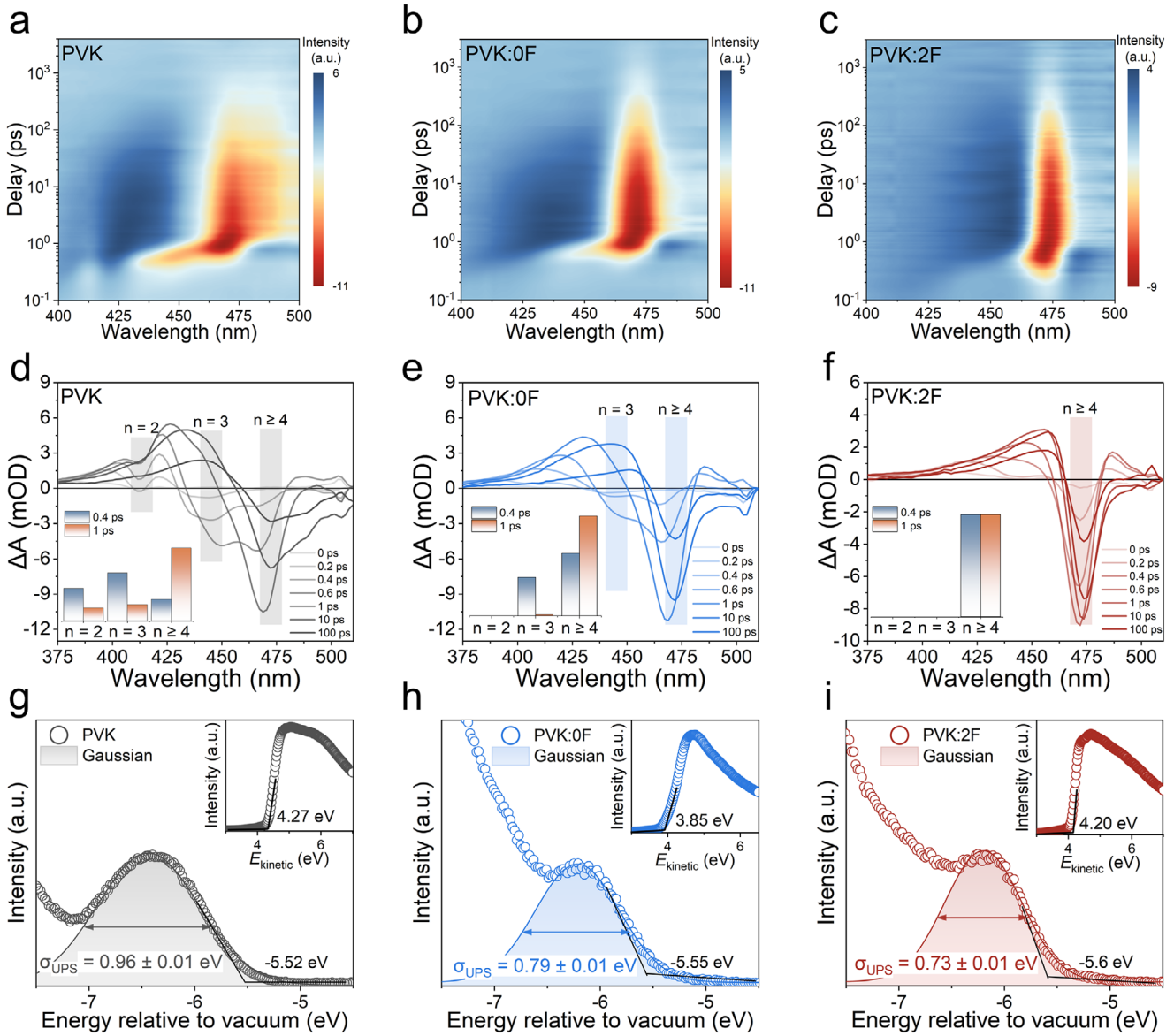

FIGURE 3 | Phase distribution, energy funneling, and energetic disorder regulated by D–A molecules. (a–c) Femtosecond transient absorption (fs-TA) 2D maps of perovskite films on PVK, PVK:0F and PVK:2F. (d–f) fs-TA spectra at selected delay times; insets show relative carrier populations of different n phases at 0.4 and 1 ps. (g–i) Ultraviolet photoelectron spectroscopy (UPS) valence-band spectra with fitted HOMO-onset width (σ_{UPS}); insets show secondary electron cutoff spectra and work functions.

and PVK:0F, indicating altered recombination dynamics and suppressed nonradiative decay (Figure 4c).

To quantify these changes, the radiative recombination rate (k_r) and nonradiative recombination rate (k_{nr}) were estimated from the PLQY and lifetime data (Figure 4i and Table S1). The analysis shows that 2F slightly increases k_r but substantially decreases k_{nr}, further indicating that enhanced luminescence mainly arises from suppressed defect-related nonradiative losses.

To further clarify the roles of temperature-dependent nonradiative losses and electron–phonon coupling in the emission process, we investigated the excitonic dynamics of the different perovskite films using temperature-dependent 2D PL maps (Figure 4d–f and Figure S12). The integrated PL intensity was then plotted as a function of temperature and fitted with the Arrhenius equation to extract the corresponding exciton binding energies (E_b): [39]

$$I(T) = \frac{I_0}{1 + A\ \exp\left(-\frac{E_b}{k_B T}\right)}$$

Here, I_0 is the integrated PL intensity at 0 K, A is a proportionality constant, and k_B is the Boltzmann constant. In this context, E_b represents the energy barrier against exciton dissociation into free carriers or nonradiative annihilation through trap states.

The extracted E_b values are 49.7, 66.9, and 74.9 meV for the PVK, PVK:0F, and PVK:2F samples, respectively (Figure 4g). The larger E_b of the 2F-modified film indicates greater resistance of excitons to thermal activation, which helps suppress thermally induced nonradiative losses. We further analyzed the

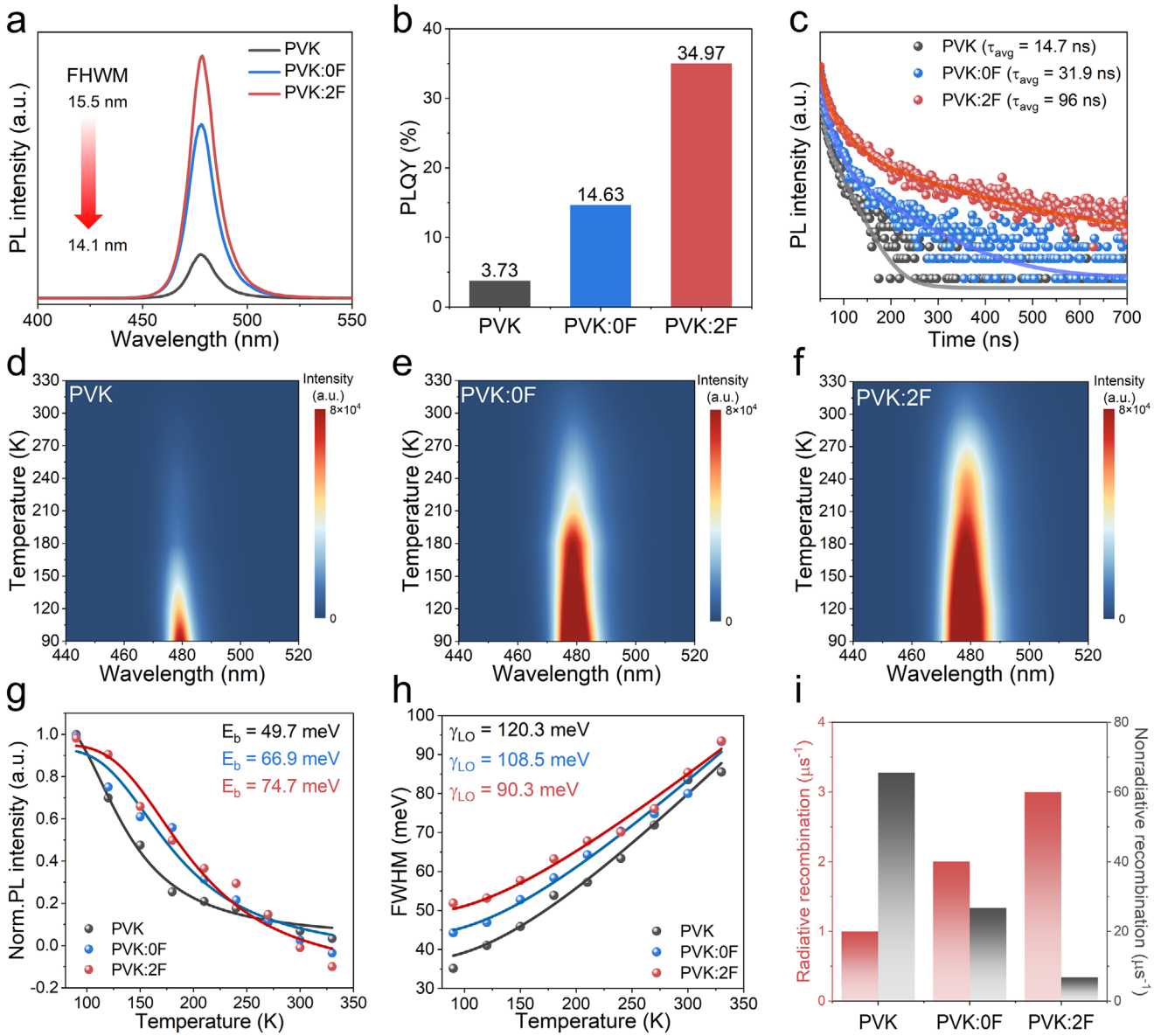

FIGURE 4 | Photophysical dynamics and thermal emission evolution of perovskite films. (a) Steady-state photoluminescence (PL) spectra. (b) Photoluminescence quantum yield (PLQY) statistics. (c) Time-resolved PL (TRPL) decay curves and average lifetimes. (d–f) Temperature-dependent PL 2D maps. (g,h) Fitted exciton binding energy (E_b) and electron-phonon coupling strength (γ_{LO}). (i) Radiative/nonradiative recombination rates from PLQY and TRPL data.

temperature dependence of the emission linewidth by plotting the FWHM as a function of temperature and fitting the data with the Fröhlich longitudinal optical phonon coupling model to quantify the electron-phonon coupling strength (γ_{LO}): [40]

$$\Gamma(T) = \Gamma_0 + \gamma_{ac}T + \frac{\gamma_{LO}}{exp(\frac{E_{LO}}{k_BT}) - 1}$$

Here, Γ_0 is the FWHM of the zero-phonon line at absolute zero, γ_{ac} describes exciton coupling to acoustic phonons, and E_{LO} is the optical phonon energy. As the acoustic phonon coupling γ_{ac} is weak compared with γ_{LO} in lead halide perovskites, γ_{ac} is neglected in the present fitting [41]. The fitted γ_{LO} values decrease from 120.3 meV for PVK to 108.5 meV for PVK:0F and 90.3 meV for PVK:2F. This reduction indicates weaker Fröhlich interaction in the 2F-modified film, consistent with molecular bridge induced defect passivation and improved energetic order.

To evaluate the device-level effects of the D–A molecular bridges at the buried interface, we fabricated blue PeLEDs based on this interfacial design. This strategy was intended to promote perovskite crystallization, suppress energetic disorder in PVK, and regulate the distribution of low-n phases. The corresponding energy-level alignment is presented in Figure 5a, with the energy levels of PVK, PVK:0F, and PVK:2F determined by UPS measurements (Figure S13). Both 0F and 2F shift the HOMO level of PVK and improve its alignment with the perovskite, helping to reduce the hole injection barrier and facilitate charge transport. The device architecture is ITO/PTAA/PVK:0F or PVK:2F/perovskite/PO-T2T/LiF/Al (Figure 5b).

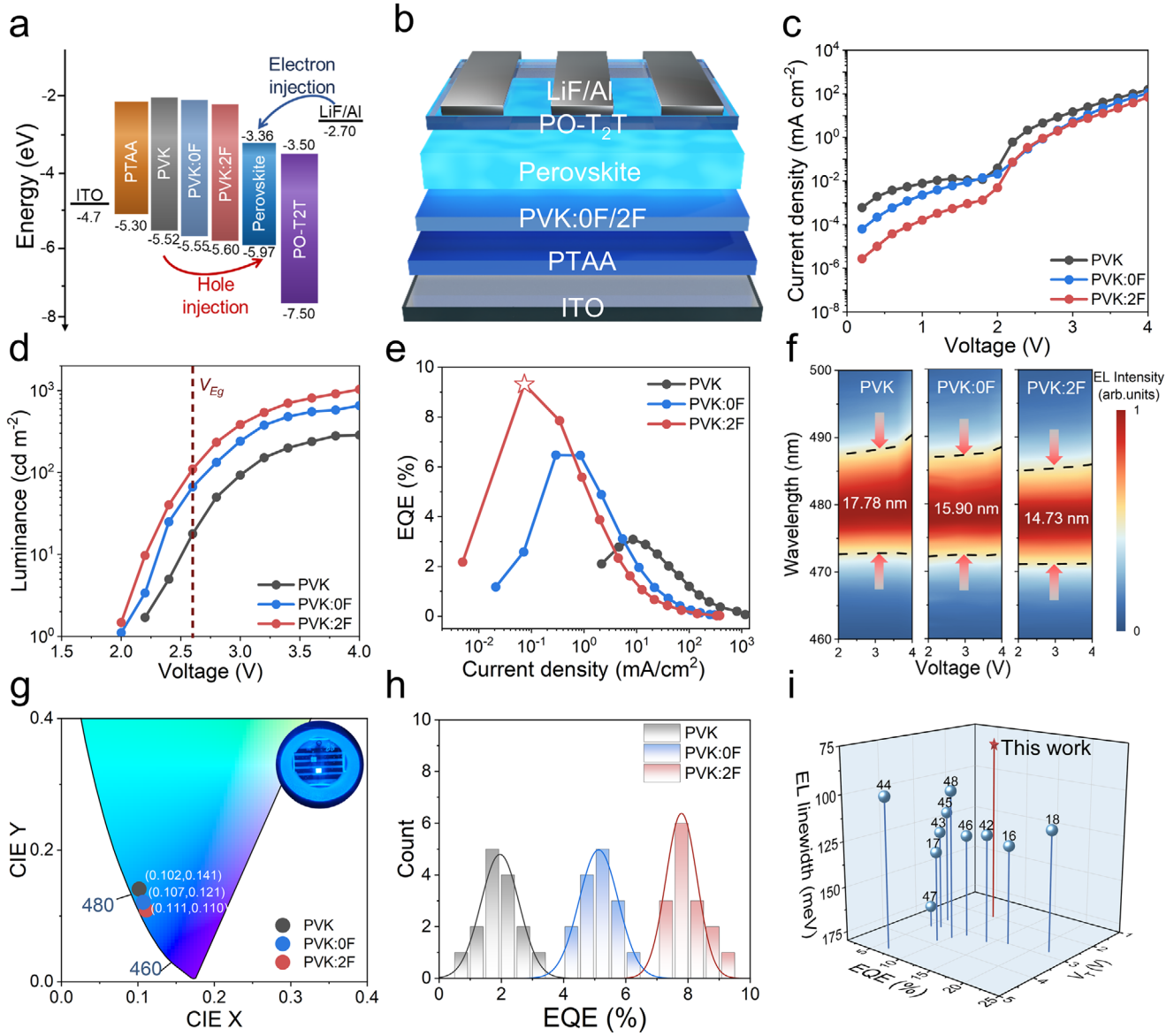

FIGURE 5 | Device performance of molecular bridge blue PeLEDs. (a) Energy-level diagram. (b) Device architecture. (c) Current density–voltage, (d) luminance–voltage, and (e) EQE–current density curves. (f) Bias-dependent EL spectra and FWHM evolution. (g) CIE coordinates; inset, operating device at 4 V. (h) EQE statistics. (i) Comparison with reported 470–480 nm quasi-2D blue PeLEDs in EQE, V_T, and EL linewidth.

Relative to the PVK device, the 2F-modified device exhibits lower leakage current, lower V_T, and higher luminance, reaching a maximum of 1034 cd m^{-2} (Figure 5c,d). These improvements indicate suppressed defect-related losses at the buried interface together with more balanced charge injection and transport. Devices incorporating 0F or 2F both show a V_T of 2.0 V, below the bandgap voltage of the emissive layer (E_g = 2.6 eV), suggesting that efficient radiative recombination can be established at low bias. This low-V_T operation can be attributed to reduced interfacial defects, suppressed energetic disorder, lower hole-injection losses, and efficient recombination in the dominant emissive phase.

These interfacial advantages lead to clear improvements in device efficiency and spectral purity. The maximum EQE rises from 3.0% in the control device to 9.3% in the 2F-based device (Figure 5e). At the same time, the EL peak remains nearly unchanged at 478 nm, while the FWHM decreases from 17.78 to 14.73 nm, indicating improved blue color purity (Figure 5f). The corresponding Commission Internationale de l'Eclairage (CIE) coordinates are shown, with the inset displaying bright blue emission from the device under a 4 V bias (Figure 5g). In addition, the 2F-modified device shows less variation in bias-dependent CIE coordinates, confirming better color stability during operation (Figure S14). The PVK:2F devices also show good reproducibility, with 15 independent devices achieving an average EQE of 6.38 ± 1.2% (Figure 5h). Interfacial molecular modification also enhances operational stability, as the PVK:2F device shows a T_{50} of 41.9 min at 100 cd m^{-2}, compared with 4.5 and 11.7 min for PVK and PVK:0F, respectively (Figure S15). This result shows that the D-A molecules not only enhance electroluminescent performance, but also markedly slow device degradation. Benchmarking against reported 470–480 nm quasi-2D blue PeLEDs [16–18, 42–48] shows that most devices exhibit an EL linewidth above 100

meV and a V_T over 3 V (Figure 5i), whereas PVK:2F combines an ultranarrow EL linewidth of 80 meV (14.73 nm), a V_T of 2.0 V, and a maximum EQE of 9.3%. The simultaneous reduction in EL linewidth and turn-on voltage suggests that D–A molecular-bridge design narrows the emissive phase distribution, reduces interfacial energy losses, and facilitates charge injection. These results highlight molecular engineering of buried interfaces as a useful strategy for developing blue PeLEDs with low turn-on voltage and high color purity.

3 | Conclusions

In summary, we demonstrate a multifunctional D–A molecular bridge strategy for buried interface regulation in blue quasi-2D PeLEDs. By incorporating the D–A molecules 0F and 2F into the PVK hole transport layer, molecular bridges are formed at the PVK/perovskite interface. π–π interactions between the D–A molecules and PVK reduce energetic disorder in the HTL and facilitate hole transport, while carboxylate coordination with undercoordinated Pb^{2+} promotes interfacial nucleation, crystallization, and defect passivation. In 2F, hydrogen bonding between fluorinated sites and PEA^+ suppresses low-n phases, promotes energy funneling, and reduces nonradiative recombination. Consequently, the 2F-modified device delivers blue emission at 478 nm with a maximum EQE of 9.3%, an ultranarrow EL linewidth of 80 meV (14.73 nm) and a T_{50} operational lifetime of 41.9 min at 100 cd m^{-2}. Overall, this work establishes D–A molecular bridge interface engineering as an effective strategy for low-voltage, ultranarrow and operationally stable blue PeLEDs.

Acknowledgements

This research was supported by the National Natural Science Foundation of China (52102159, 52572155, 52272141, and 52573244), and the Natural Science Foundation of Fujian Province (2025J01655 and 2024J02014).

Conflicts of Interest

The authors declare no conflicts of interest.

Data Availability Statement

The data that support the findings of this study are available from the corresponding author upon reasonable request.

References

1. H. Li, X. Zhu, D. Zhang, et al., "Thermal Management Towards Ultra-Bright and Stable Perovskite Nanocrystal-Based Pure Red Light-Emitting Diodes," *Nature Communications* 15 (2024): 6561, https://doi.org/10.1038/s41467-024-50634-0.

2. M. Li, Y. Yang, Z. Kuang, et al., "Acceleration of Radiative Recombination for Efficient Perovskite LEDs," *Nature* 630 (2024): 631–635, https://doi.org/10.1038/s41586-024-07460-7.

3. D. Zhu, Y. Zhou, X. Wen, et al., "Deep-Blue Light-Emitting Diodes Based on Perovskite Single-Crystal Thin Films," *Science Advances* 11 (2025): adz8060, https://doi.org/10.1126/sciadv.adz8060.

4. H. Li, Y. Feng, M. Zhu, et al., "Nanosurface-Reconstructed Perovskite for Highly Efficient and Stable Active-Matrix Light-Emitting Diode Display," *Nature Nanotechnology* 19 (2024): 638–645, https://doi.org/10.1038/s41565-024-01652-y.

5. W. Bai, T. Xuan, H. Zhao, et al., "Perovskite Light-Emitting Diodes With an External Quantum Efficiency Exceeding 30%," *Advanced Materials* 35 (2023): 2302283, https://doi.org/10.1002/adma.202302283.

6. R. Chen, Z. Wang, S. Zheng, et al., "Carbon Dots: Electroluminescent Devices for Lighting and Display Applications," *eScience* 6 (2025): 100517, https://doi.org/10.1016/j.esci.2025.100517.

7. S. Yuan, L. Dai, Y. Sun, et al., "Efficient Blue Electroluminescence From Reduced-Dimensional Perovskites," *Nature Photonics* 18 (2024): 425–431, https://doi.org/10.1038/s41566-024-01382-6.

8. Z. Li, Z. Chen, Z. Shi, et al., "Charge Injection Engineering at Organic/Inorganic Heterointerfaces for High-Efficiency and Fast-Response Perovskite Light-Emitting Diodes," *Nature Communications* 14 (2023): 6441, https://doi.org/10.1038/s41467-023-41929-9.

9. H. Qi, H. Wang, Y. Chen, et al., "Synchronous Optimization of Light Outcoupling and Carrier Recombination for Efficient and Spectral Stable Blue Perovskite Light-Emitting Diodes," *Advanced Functional Materials* 34 (2024): 2400052, https://doi.org/10.1002/adfm.202400052.

10. M. Yuan, L. N. Quan, R. Comin, et al., "Perovskite Energy Funnels for Efficient Light-Emitting Diodes," *Nature Nanotechnology* 11 (2016): 872–877, https://doi.org/10.1038/nnano.2016.110.

11. S. Liu, Z. Guo, X. Wu, et al., "Zwitterions Narrow Distribution of Perovskite Quantum Wells for Blue Light-Emitting Diodes With Efficiency Exceeding 15%," *Advanced Materials* 35 (2023): 2208078, https://doi.org/10.1002/adma.202208078.

12. X. Yang, L. Ma, M. Yu, et al., "Focus on Perovskite Emitters in Blue Light-Emitting Diodes," *Light: Science & Applications* 12 (2023): 177, https://doi.org/10.1038/s41377-023-01206-2.

13. M. Karlsson, Z. Yi, S. Reichert, et al., "Mixed Halide Perovskites for Spectrally Stable and High-Efficiency Blue Light-Emitting Diodes," *Nature Communications* 12 (2021): 361, https://doi.org/10.1038/s41467-020-20582-6.

14. Y. Yu, B.-F. Wang, Y. Shen, et al., "Efficient Blue Perovskite LEDs via Bottom-Up Charge Manipulation for Solution-Processed Active-Matrix Displays," *Advanced Materials* 37 (2025): 2503234, https://doi.org/10.1002/adma.202503234.

15. S. Ding, Q. Wang, W. Gu, et al., "Phase Dimensions Resolving of Efficient and Stable Perovskite Light-Emitting Diodes at High Brightness," *Nature Photonics* 18 (2024): 363–370, https://doi.org/10.1038/s41566-023-01372-0.

16. Z. Chu, W. Zhang, J. Jiang, et al., "Blue Perovskite Light-Emitting Diodes Using Multifunctional Small Molecule Dopants," *Advanced Materials* 37 (2025): 2409718, https://doi.org/10.1002/adma.202409718.

17. X. Zhou, Z. Ren, Z. Zheng, et al., "Efficient and Stable Blue Perovskite Light-Emitting Diodes Enabled by Effective Hydrolysis of Dichloride," *Advanced Functional Materials* 35 (2024): 2412894, https://doi.org/10.1002/adfm.202412894.

18. H. Qi, Y. Tong, X. Zhang, et al., "Homogenizing Energy Landscape for Efficient and Spectrally Stable Blue Perovskite Light-Emitting Diodes," *Advanced Materials* 36 (2024): 2409319, https://doi.org/10.1002/adma.202409319.

19. F. Zhang, Y. Gao, P. Lu, et al., "Engineering of Hole Transporting Interface by Incorporating the Atomic-Precision Ag_6 Nanoclusters for High-Efficiency Blue Perovskite Light-Emitting Diodes," *Nano Letters* 23 (2023): 1582–1590, https://doi.org/10.1021/acs.nanolett.3c00068.

20. M. Yu, T. Qin, G. Gao, et al., "Charge Environment and Perovskite Crystallization Regulation Interface Engineering With Molecular Bridge for Efficient Deep-Blue (448 nm) Light-Emitting Diodes," *ACS Nano* 19 (2025): 39181–39191, https://doi.org/10.1021/acsnano.5c12388.

21. Q. Liao, Y. Wang, Z. Zhang, et al., "Self-Assembled Donor-Acceptor Hole Contacts for Inverted Perovskite Solar Cells With an Efficiency Approaching 22%: The Impact of Anchoring Groups," *Journal of Energy Chemistry* 68 (2022): 87–95, https://doi.org/10.1016/j.jechem.2021.11.001.

22. J. Zhu, Y. Luo, R. He, et al., "A Donor–Acceptor-Type Hole-Selective Contact Reducing Non-Radiative Recombination Losses in both Subcells towards Efficient All-Perovskite Tandems," *Nature Energy* 8 (2023): 714–724, https://doi.org/10.1038/s41560-023-01274-z.

23. Y. Wang, Q. Liao, J. Chen, et al., "Teaching an Old Anchoring Group New Tricks: Enabling Low-Cost, Eco-Friendly Hole-Transporting Materials for Efficient and Stable Perovskite Solar Cells," *Journal of the American Chemical Society* 142 (2020): 16632–16643, https://doi.org/10.1021/jacs.0c06373.

24. Y. Xia, C. Zou, Y.-H. Lou, et al., "Screening Fluorination Additives for Efficient Perovskite Light-Emitting Diodes," *Advanced Materials* 37 (2025): 2411231, https://doi.org/10.1002/adma.202411231.

25. J. Zhu, X. Huang, Y. Luo, et al., "Self-Assembled Hole-Selective Contact for Efficient Sn-Pb Perovskite Solar Cells and All-Perovskite Tandems," *Nature Communications* 16 (2025): 240, https://doi.org/10.1038/s41467-024-55492-4.

26. J. Dong, B. Zhao, H. Ji, et al., "Multivalent-Effect Immobilization of Reduced-Dimensional Perovskites for Efficient and Spectrally Stable Deep-Blue Light-Emitting Diodes," *Nature Nanotechnology* 20 (2025): 507–514, https://doi.org/10.1038/s41565-024-01852-6.

27. X. Wu, Z. Wang, S. Zheng, et al., "Stabilizing the Buried Interface Phase for Perovskite LEDs With a Remarkable T_{90} Lifetime at 1000 Nit," *Nano Letters* 25 (2025): 18158–18166, https://doi.org/10.1021/acs.nanolett.5c05743.

28. J. Huang, X. Li, Z. Zhang, et al., "Oriented Crystallization of Perovskite Film via Fluorine-Containing Hyperbranched Polymer for Efficient and Stable Perovskite Solar Cells," *Advanced Materials* 38 (2026): 11684, https://doi.org/10.1002/adma.202511684.

29. D. Ma, K. Lin, Y. Dong, et al., "Distribution Control Enables Efficient Reduced-Dimensional Perovskite LEDs," *Nature* 599 (2021): 594–598, https://doi.org/10.1038/s41586-021-03997-z.

30. S. Zheng, Z. Wang, N. Jiang, et al., "Ultralow Voltage–driven Efficient and Stable Perovskite Light-Emitting Diodes," *Science Advances* 10 (2024): adp8473, https://doi.org/10.1126/sciadv.adp8473.

31. S. Wang, Z. Yu, J. Qin, et al., "Buried Interface Modification and Light Outcoupling Strategy for Efficient Blue Perovskite Light-Emitting Diodes," *Science Bulletin* 69 (2024): 2231–2240, https://doi.org/10.1016/j.scib.2024.05.028.

32. B. Li, Q. Liu, J. Gong, et al., "Harnessing Strong Aromatic Conjugation in Low-Dimensional Perovskite Heterojunctions for High-Performance Photovoltaic Devices," *Nature Communications* 15 (2024): 2753, https://doi.org/10.1038/s41467-024-47112-y.

33. X. Zhang, Z. Liu, L. Wang, et al., "Manipulating Charge Transfer Dynamics and Stabilizing Lead Bromide Octahedra for Efficient Blue Perovskite Light-Emitting Diodes," *Nature Communications* 17 (2026): 1610, https://doi.org/10.1038/s41467-026-68315-5.

34. S. Zheng, Z. Wang, G. Zheng, et al., "Stable Sky-Blue Perovskite LEDs Achieved by Efficient Sub-Bandgap Emission With 24.5% PCE," *Advanced Functional Materials* 36 (2025): 21079, https://doi.org/10.1002/adfm.202521079.

35. J. S. Kim, H.-D. Lee, J. H. Jung, et al., "Kinetically-Controlled Intermediate-Direct-Pinning for Homogeneous Energy Landscapes in Quasi-Two-Dimensional Perovskites for Efficient and Narrow Blue Emission," *Nature Communications* 16 (2025): 9590, https://doi.org/10.1038/s41467-025-62863-y.

36. L. Kong, X. Zhang, Y. Li, et al., "Smoothing the Energy Transfer Pathway in Quasi-2D Perovskite Films Using Methanesulfonate Leads to Highly Efficient Light-Emitting Devices," *Nature Communications* 12 (2021): 1246, https://doi.org/10.1038/s41467-021-21522-8.

37. Z. Luo, W. Zheng, Y. Hua, et al., "Energetic Disorder Mitigation of Hole-Transport Layers via Molecular Assembly Boosts Charge Transport to Unlock Efficient and Stable Perovskite Light-Emitting Devices," *Nano Letters* 25 (2025): 17112–17121, https://doi.org/10.1021/acs.nanolett.5c04553.

38. Y. Deng, F. Peng, Y. Lu, et al., "Solution-Processed Green and Blue Quantum-Dot Light-Emitting Diodes With Eliminated Charge Leakage," *Nature Photonics* 16 (2022): 505–511, https://doi.org/10.1038/s41566-022-00999-9.

39. Z. Wang, S. Zheng, N. Jiang, et al., "Minimizing Interfacial Energy Losses With Carbon Dot Bifacial Modification Layers for High-Efficiency and Stable Perovskite LEDs," *Advanced Functional Materials* 35 (2025): 2423608, https://doi.org/10.1002/adfm.202423608.

40. M. Fu, P. Tamarat, J.-B. Trebbia, et al., "Unraveling Exciton–Phonon Coupling in Individual FAPbI3 Nanocrystals Emitting Near-Infrared Single Photons," *Nature Communications* 9 (2018): 3318, https://doi.org/10.1038/s41467-018-05876-0.

41. Q. Wang, Y. Chen, C. Yan, et al., "Molecularly Designing a Passivation ETL to Suppress EQE Roll-Off of PeLEDs," *ACS Energy Letters* 8 (2023): 3710–3719, https://doi.org/10.1021/acsenergylett.3c01379.

42. L. Zhang, Y. Jiang, Y. Feng, et al., "Manipulating Local Lattice Distortion for Spectrally Stable and Efficient Mixed-Halide Blue Perovskite LEDs," *Angewandte Chemie, International Edition* 135 (2023): 202302184, https://doi.org/10.1002/anie.202302184.

43. L. Liu, J. Piao, Y. Wang, et al., "Trifunctional Trichloroacetic Acid Incorporated Mixed-Halide Perovskites for Spectrally Stable Blue Light-Emitting Diodes," *The Journal of Physical Chemistry Letters* 14 (2023): 4734–4741, https://doi.org/10.1021/acs.jpclett.3c01028.

44. J. J. Do and J. W. Jung, "Strategic Buried Defect Passivation of Perovskite Emitting Layers by Guanidinium Chloride for High-Performance Pure Blue Perovskite Light Emitting Diodes," *Small* 20 (2024): 2400544, https://doi.org/10.1002/smll.202400544.

45. Y. Seop Shin, Y. Jin Yoon, S. Hyeon Kweon, et al., "Controlling the Formation Energy of Perovskite Phase via Surface Polarity of Substrate for Efficient Pure-Blue Light-Emitting Diodes," *Chemical Engineering Journal* 464 (2023): 142707, https://doi.org/10.1016/j.cej.2023.142707.

46. Y. S. Shin, C. B. Park, A. Adhikari, et al., "Manipulated Interface for Enhanced Energy Cascade in Quasi-2D Blue Perovskite Light-Emitting Diodes," *ACS Energy Letters* 7 (2022): 3345–3352, https://doi.org/10.1021/acsenergylett.2c01785.

47. S. Park, J. Kim, G.-M. Kim, et al., "Controlling the Phase Distribution of Single Bromide Quasi-2-Dimensional Perovskite Crystals via Solvent Engineering for Pure-Blue Light-Emitting Diodes," *ACS Applied Materials & Interfaces* 16 (2024): 38395–38403, https://doi.org/10.1021/acsami.4c06778.

48. Y. Yang, S. Xu, Z. Ni, et al., "Highly Efficient Pure-Blue Light-Emitting Diodes Based on Rubidium and Chlorine Alloyed Metal Halide Perovskite," *Advanced Materials* 33 (2021): 2100783, https://doi.org/10.1002/adma.202100783.

Supporting Information

Additional supporting information can be found online in the Supporting Information section.

Supporting File: lpor71829-sup-0001-SuppMat.docx.